Chemical Engineering Journal 470 (2023) 144251

Contents lists available at ScienceDirect

Chemical Engineering Journal

journal homepage: www.elsevier.com/locate/cej

Optimization of an electrochemical direct air capture process with decreased CO_2 desorption pressure and addition of background electrolyte

Qingdian Shu [a,b,*], Ching Shing Sin [a,b], Michele Tedesco [a], Hubertus V.M. Hamelers [a,b], Philipp Kuntke [a,b,*]

[a] Wetsus, European Centre of Excellence for Sustainable Water Technology, Oostergoweg 9, 8911MA Leeuwarden, the Netherlands
[b] Environmental Technology, Wageningen University & Research, Bornse Weilanden 9, 6708WG Wageningen, the Netherlands

ARTICLE INFO

Keywords:
Direct air capture
Electrochemical cell
pH swing
Partial vacuum
Background electrolyte

ABSTRACT

An electrochemical process based on pH-swing has been proposed recently to regenerate spent alkaline absorbent from direct air capture (DAC). In this work, we experimentally investigated and theoretically simulated two optimization strategies to further reduce the energy consumption of such novel electrochemical process. First, partial vacuum was applied to the gas phase during CO_2 desorption to increase the gas production rate. The energy consumption of the electrochemical cell decreased by 12 to 15% when the CO_2 partial pressure in the gas phase was reduced from 0.9 to 0.3 atm. Second, phosphate and sulphate were tested as background electrolyte to the alkaline absorbent, reducing the energy consumption by minimizing the ohmic losses in the electrochemical cell. The optimal concentration for phosphate was 0.1 M, while the CO_2 production rate was limited by either the total carbon feeding rate or the high acidifying solution pH at higher concentrations of phosphate. Moreover, due to the low pKa and high molar conductivity of sulphate compared to phosphate, sulphate addition showed an even lower energy consumption than phosphate addition. Finally, the lowest experimental energy consumption was 247 kJ mol^{-1} CO_2 achieved with CO_2 partial pressure of 0.3 atm and 0.1 M of sulphate addition at current density of 150 A m^{-2} while our mathematical model predicted a theoretical minimum energy consumption of 138 kJ mol^{-1} under the same condition. Overall, the investigated optimization strategies advanced the development of an energy-efficient electricity-driven process for direct air capture.

1. Introduction

Climate change caused by anthropogenic emissions of greenhouse gases is one of the biggest threats of the century [1]. The atmospheric carbon dioxide (CO_2) concentration has increased by 50% comparing to pre-industrial level [2]. The heat-trapping nature of CO_2 has warmed the atmosphere, ocean, and land, which leads to vital signs of global warming, e.g., shrinking ice sheets, rising sea level, and more extreme natural events [3–5]. In response to the escalating impacts of climate change, carbon dioxide removal (CDR), aiming explicitly to reduce CO_2 levels from the atmosphere, has emerged as a crucial process that helps achieve carbon neutrality and provides opportunities for negative CO_2 emissions [6–8]. Direct air capture (DAC), a promising strategy of CDR, aims to produce high-purity CO_2 stream from ambient air via an adsorption/desorption cycle [9–11]. Although the low CO_2 concentration in the air makes DAC thermodynamically unfavourable comparing to other carbon capture processes from more CO_2-concentrated gas streams, DAC has the advantage of high flexibility in operation location, and the deployment of DAC technologies is critical for urgently mitigating the rapid climate change [12,13].

DAC with liquid alkaline absorbent and regeneration using a thermal swing has been demonstrated by Keith et al. [14]. Alternative electrochemical regeneration processes have been proposed to replace the consumption of thermal energy by electricity [15–18]. Several groups have studied using bipolar membrane electrodialysis (BPMED) to create a pH swing so that CO_2 is evolved from the spent absorbent under a low pH while the alkaline absorbent is regenerated under a high pH [19–22]. We recently showed the simultaneous CO_2 desorption and regeneration of spent DAC alkaline absorbent utilizing a H_2-recycling electrochemical system [23,24]. In this electrochemical system, H_2 is oxidized to protons (H^+) at the anode. The produced protons reduce the pH of the spent alkaline absorbent so that the carbonate (CO_3^{2-}) and bicarbonate (HCO_3^-) ions in solution are converted into carbonic acid (H_2CO_3*, including dissolved CO_2). When the solution is saturated with carbonic acid, CO_2

* Corresponding authors at: Environmental Technology, Wageningen University & Research, Bornse Weilanden 9, 6708WG Wageningen, the Netherlands.
E-mail addresses: qingdian.shu@wetsus.nl (Q. Shu), philipp.kuntke@wur.nl (P. Kuntke).

https://doi.org/10.1016/j.cej.2023.144251
Received 22 February 2023; Received in revised form 11 May 2023; Accepted 18 June 2023
Available online 19 June 2023

gas evolves and is separated from the liquid solution. The CO_2-depleted solution is reduced at cathode where the alkaline absorbent is regenerated due to the production of hydroxide ion (OH^-). The reduction reaction at cathode also produces H_2 that can compensate for the H_2 consumption at anode.

Using such electrochemical DAC design, we have previously reached an energy consumption of 374 kJ mol^{-1} CO_2 under 50 A m^{-2}, while model predictions suggested a theoretical minimum as low as 164 kJ mol^{-1} CO_2 under same conditions [23]. The low energy consumption made this process competitive compared to the state of the art, such as the calciner thermal cycle process assessed by Keith et al. (338 kJ mol^{-1} CO_2) [14] and the bipolar membrane electrodialysis process evaluated by Sabatino et al. (236 kJ mol^{-1} CO_2) [25]. However, the gap between the experimental and simulated energy consumption implies an optimization potential. Therefore, in this work, we aim to investigate two operational strategies to reduce the energy consumption of the proposed DAC process.

The energy consumption of the process is inversely proportional to the CO_2 production rate and proportional to the electric power of the electrochemical cell. The CO_2 production rate is determined by the driving force for CO_2 desorption that originates from the difference between the dissolved CO_2 concentration and the CO_2 partial pressure in the gas phase, and lower CO_2 partial pressure in the gas phase facilitates the desorption of CO_2 from liquid phase to gas phase [26,27]. Therefore, in this work, we attempted to increase the CO_2 production rate of the electrochemical cell by applying partial vacuum to the gas phase during the desorption step. Moreover, we also showed the impact of reduced CO_2 partial pressure in the gas phase on the performance of the electrochemical cell under different operational conditions.

Under galvanostatic (i.e., constant current) conditions, the power of the electrochemical cell is dominated by the potential drop over the cell. The potential drop largely depends on the ohmic resistance of the solutions and the electrode overpotentials. In this regard, we added background electrolytes in different concentrations and forms to the absorbent to increase the ionic conductivity and studied the effect on the performance of the system. Sabatino et al. simulated the addition of inert salt in a bipolar membrane electrodialysis DAC process and showed the benefit of reducing the energy consumption [28]. Furthermore, Jeremiasse et al. demonstrated that the concentration overpotential for hydrogen evolution was reduced in the presence of buffer [29]. Thus, we compared one background electrolyte with buffer capacity (phosphate) and one without buffer capacity (sulphate) to explore the difference in system performance under different operational conditions.

2. Materials and methods

2.1. Experimental setup

The electrochemical cell consisted of three compartments, i.e., anode compartment, acidifying compartment, and cathode compartment, enclosed by two poly(methyl methacrylate) (PMMA) endplates (21 cm × 21 cm × 2.5 cm) (Fig. 1). Two Ru/Ir-coated titanium mesh electrodes (9.8 cm × 9.8 cm) were used, one as the cathode and the other as the current collector for the anode. The anode was a membrane electrode assembly (MEA) (FuelCellsEtc, USA) comprising a gas diffusion layer (GDL) (10 cm × 10 cm), coated by a Platinum-Vulcan (carbon) catalyst (0.5 mg Pt cm^{-2}), incorporated with a Nafion N117 cation exchange membrane (CEM) (15 cm × 15 cm). The GDL and CEM sides of the MEA faced the anode and acidifying compartments, respectively. The acidifying and cathode compartments were separated by an additional CEM (15 cm × 15 cm, Fumasep FKB-PK-75, FUMATECH, Germany), and two polymeric nitrile spacers (500 μm thick, Sefar, Switzerland) were used to create the flow channel for these two compartments.

Two circulation loops were used for the acidifying and cathode compartments, respectively. In each circulation loop, the outlet from the cell was directed into a hollow fibre membrane contactor (Liqui-Cel™ EXF-2.5 × 8, 3M, USA), where the produced CO_2 (or H_2) gas could be separated, and the liquid stream from the membrane contactor flowed back into the cell. The influent of the system, which was the spent alkaline absorbent, was mixed with the acidifying solution before entering the acidifying compartment. While the overflow of acidifying solution flowed into the mixing vessel in the catholyte circulation loop, the overflow of surplus catholyte left the circulation as effluent. Three peristaltic pumps (Masterflex L/S, Metrohm Applikon BV, the Netherlands) were installed in the system, one for the influent and two for the two circulation loops (800 mL min^{-1}). Two additional peristaltic pumps (Masterflex L/S, Metrohm Applikon BV, the Netherlands) were connected to the gas outlets of the membrane contactors to maintain the

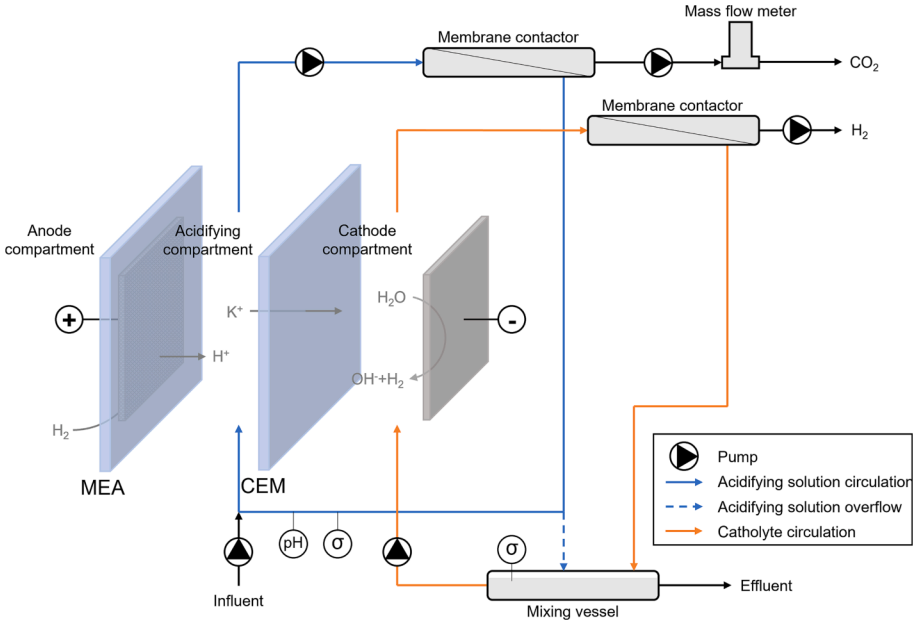

Fig. 1. Schematic representation of the process with electrochemical regeneration of alkaline DAC absorbent. Influent: spent alkaline absorbent from the absorber. Effluent: regenerated absorbent to send to the absorber. MEA = membrane electrode assembly, CEM = cation exchange membrane.

desired air pressure, which was measured by two manometers (Cerabar PMP21, Endress + Hauser, Germany; MAN-SD1S, Kobold Messering GmbH, Germany). The gas side of the membrane contactor in the catholyte circulation loop was kept at a gas pressure of 0.70 atm to enhance the removal efficiency of H_2 and avoid gas entrained in the cell through the circulation loop. In the CO_2 gas stream, the water vapor of the separated gas was removed via a Nafion tubing (TUB-0003, CO2Meter.com, USA). The gas production rate was recorded by a mass flow meter (EL-FLOW Prestige FG-111B, Bronkhorst, the Netherlands). Gas samples were taken from the setup during experiments, and their compositions were analyzed by gas chromatography (μGC, Varian CP-4900, Agilent, USA). Although the H_2 produced at the cathode could be directly recirculated to the anode, a tailor-made electrolyzer was used to feed H_2 to the anode for simplicity.

A galvanostatic/potentiostat (IviumStat, Ivium, the Netherlands) was connected to the cell to apply a constant current. Two saturated calomel reference electrodes (+0.244 V vs SHE, QM712X, ProSense BV, the Netherlands) were placed at the inlets of the acidifying and cathode compartments to measure the anode and cathode potentials. A multimeter (8846A, Fluke, the Netherlands) was connected between the two reference electrodes to measure the potential difference across the acidifying and cathode compartments. The conductivities of the acidifying and catholyte solutions were measured by two conductivity sensors (Memosens CLS82D, Endress + Hauser BV, the Netherlands) placed in the two circulation loops, while the pH of the acidifying solution was measured by a pH sensor (Orbisint CPS11D, Endress + Hauser BV, the Netherlands). The concentrations of ions in the influent, the acidifying solution, and the catholyte solution were measured by ion chromatography (761 Compact IC, Metrohm, Switzerland).

2.2. Experimental procedure

The experiments were operated in a continuous mode with the influent solution constantly feeding into the acidifying circulation loop until the complete system reached steady-state. The influent solutions for the electrochemical system resembled spent potassium hydroxide absorbents. The composition is determined by the equilibrium between 400 ppm of CO_2 under atmospheric pressure and the alkaline absorbent based on Henry's law and the equilibria of species in the liquid phase. The equilibria change with different K^+ concentrations, different background electrolyte addition, and different concentrations of the background electrolyte. The detailed compositions of all the influent solutions are listed in Table S1.

To evaluate the performance of the system under different fluid dynamic and current conditions, we defined the "K^+ load ratio" (L_{K^+}) as a control parameter to describe the ratio between the applied current density and the K^+ loading rate:

$$L_{K^+} = \frac{j_c \cdot A}{c_{K^+,0} \cdot Q \cdot F} \tag{1}$$

where j_c is the current density (A m^{-2}), A is the active membrane area (m^2), $c_{K^+,0}$ is the K^+ concentration in the influent (mol m^{-3}), Q is the influent flow rate (m^3 s^{-1}), and F is the Faraday constant (96485 C mol^{-1}).

Firstly, the effect of pressure at the gas side of the membrane contactor ($p_{CO_2,g}$) on the performance of the system was investigated. Three different conditions were selected to perform experiments with $p_{CO_2,g}$ ranging from 0.3 to 0.9 atm (Table 1). Secondly, experiments with different amount of phosphate buffer solution addition (no buffer, 0.1 M buffer, and 0.2 M buffer) were performed under the optimum $p_{CO_2,g}$ identified previously. The current density was kept constant at 150 A m^{-2}, while the influent K^+ concentration was 1.0 M. Different L_{K^+} from 0.7 to 1.1 were tested by adjusting the influent flow rate. Moreover, we have performed experiments with fixed total carbon concentration in the influent and fixed influent flow rate, to keep constant the total carbon feeding rate into the cell. In this case, the influent K^+ concentration along with the L_{K^+} were different with different amount of buffer addition. Lastly, experiments with 0.1 M sulphate addition were performed to compare with experiments with 0.1 M phosphate buffer addition under different L_{K^+}. The reported experimental results are the average values of each parameter under steady-state condition over a time period of at least 1 h.

Table 1
Different operational conditions for experiments investigating effects of pressure at the gas side of the membrane contactor ($p_{CO_2,g}$).

	Current density (A m^{-2})	L_{K^+}	Phosphate buffer (M)
Condition 1	150	0.8	0.1
Condition 2	150	0.9	0.1
Condition 3	200	0.8	0.1

2.3. Equilibrium model

An equilibrium model was developed to simulate the performance of the electrochemical cell. The simulation describes the mass transport and steady-state conditions of the acidifying and cathode compartments with some general assumptions including: i) well-mixed compartments; ii) ideal membrane behavior; and iii) no neutral species (H_2CO_3 and H_3PO_4) transport through the membrane.

2.3.1. Solution equilibrium

The solutions contain cations (K^+ and H^+), anions (OH^-, HCO_3^-, CO_3^{2-}, $H_2PO_4^-$, HPO_4^{2-}, PO_4^{3-}, and SO_4^{2-}), and neutral species (H_2CO_3 and H_3PO_4), and they are assumed to be always in acid-base equilibrium. The equilibrium constants are defined as follows:

$$K_H = \frac{c_{H_2CO_3}}{p_{CO_2(g)}} \tag{2}$$

$$K_{c1} = \frac{c_{H^+} \cdot c_{HCO_3^-}}{c_{H_2CO_3}} \tag{3}$$

$$K_{c2} = \frac{c_{H^+} \cdot c_{CO_3^{2-}}}{c_{HCO_3^-}} \tag{4}$$

$$K_{p1} = \frac{c_{H^+} \cdot c_{H_2PO_4^-}}{c_{H_3PO_4}} \tag{5}$$

$$K_{p2} = \frac{c_{H^+} \cdot c_{HPO_4^{2-}}}{c_{H_2PO_4^-}} \tag{6}$$

$$K_{p3} = \frac{c_{H^+} \cdot c_{PO_4^{3-}}}{c_{HPO_4^{2-}}} \tag{7}$$

$$K_w = c_{H^+} \cdot c_{OH^-} \tag{8}$$

where K_H is the Henry' law constant of CO_2 (mol m^{-3} atm^{-1}), K_{c1} and K_{c2} are the first and second dissociation constants of H_2CO_3 (mol m^{-3}), respectively, K_{p1}, K_{p2}, and K_{p3} are the first, second, and third dissociation constants of H_3PO_4 (mol m^{-3}), respectively, K_w is the water dissociation constant (mol^2 m^{-6}), $p_{CO_2(g)}$ is the partial pressure of CO_2 gas, and $c_{H_2CO_3}$, $c_{HCO_3^-}$, $c_{CO_3^{2-}}$, $c_{H_3PO_4}$, $c_{H_2PO_4^-}$, $c_{HPO_4^{2-}}$, $c_{PO_4^{3-}}$, c_{H^+}, and c_{OH^-} are the concentrations of corresponding ions (M), respectively.

The electroneutrality of all charged species holds in all solutions:

$$c_{K^+} + c_{H^+} = c_{OH^-} + c_{HCO_3^-} + 2 \cdot c_{CO_3^{2-}} + c_{H_2PO_4^-} + 2 \cdot c_{HPO_4^{2-}} + 3 \cdot c_{PO_4^{3-}} + 2 \cdot c_{SO_4^{2-}} \tag{9}$$

where $c_{SO_4^{2-}}$ is the concentration of SO_4^{2-} (mol m^{-3}).

The influent of the acidifying compartment is a solution in equilibrium with 1 atm 400 ppm CO_2 that consists of 1.0 M K^+. The acidifying solution is in equilibrium with a defined gas pressure in the membrane contactor (assuming pure CO_2).

Either phosphate or sulphate is added to the influent when simulating the corresponding experiments.

2.3.2. Mass transport

The applied current density determines the total flux of cations (K^+ and H^+) transported through the CEM:

$$J_{tot} = J_{K^+} + J_{H^+} = \frac{j_c}{F} \tag{10}$$

where J_{tot} is the total molar flux of cations through the CEM (mol m^{-2} s^{-1}), and J_{K^+} and J_{H^+} are the molar fluxes of K^+ and H^+ (mol m^{-2} s^{-1}), respectively.

The ion fluxes can be expressed by Nernst-Planck equation:

$$J_{K^+} = -D_{K^+} \cdot \left(\frac{dc_{K^+}}{dx} + c_{K^+,m} \frac{d\phi}{dx} \right) \tag{11}$$

$$J_{H^+} = -D_{H^+} \cdot \left(\frac{dc_{H^+}}{dx} + c_{H^+,m} \frac{d\phi}{dx} \right) \tag{12}$$

where D_{K^+} and D_{H^+} are the diffusion coefficients of K^+ and H^+ (m^2 s^{-1}), respectively, c_{K^+} and c_{H^+} are the concentrations of K^+ and H^+ at different positions inside the membrane (mol m^{-3}), respectively, $c_{K^+,m}$ and $c_{H^+,m}$ are the average concentrations of K^+ and H^+ in the membrane (mol m^{-3}), respectively, x is the position inside the membrane (m), and ϕ is the dimensionless electric potential, to be multiplied by $R \cdot T/F$ (R: ideal gas constant = 8.314 J K^{-1} mol^{-1}, T: temperature in K) to obtain the dimensional voltage.

The concentration gradient of cations over the CEM is assumed to be linear, and the boundary conditions of the membrane are not considered so that the ion concentration on the surface of the membrane equals the concentration in the bulk solution.

2.3.3. Mass balances

The mass balances of K^+ and total carbon in acidifying and cathode compartments were considered under steady-state conditions. In the acidifying compartment, the K^+ transported away equals the concentration difference between the influent ($c_{K^+,0}$, mol m^{-3}) and the acidifying solution ($c_{K^+,1}$, mol m^{-3}):

$$J_{K^+} = \frac{Q}{A} \cdot (c_{K^+,0} - c_{K^+,1}) \tag{13}$$

CO_2 is desorbed from the acidifying solution as the pH decreases. Therefore, the total carbon concentration difference between the influent ($c_{C,0}$, mol m^{-3}) and the acidifying solution ($c_{C,1}$, mol m^{-3}) corresponds to the specific CO_2 production rate (J_{CO_2}, mol m^{-2} s^{-1}):

$$J_{CO_2} = \frac{Q}{A} \cdot (c_{C,0} - c_{C,1}) \tag{14}$$

The transported K^+ and the remaining part in the acidifying solution blend in the cathode compartment, so the catholyte has the same K^+ concentration as the influent. Since no carbon species leaves the solution after the membrane contactor, the total carbon concentration in the catholyte remains as in the acidifying solution.

2.3.4. Energy consumption

This model assumes an ideal electrical behavior in the cell which neglects the electrode overpotentials and the boundary layer effects of the electrodes and membrane. Therefore, the cell voltage (E_{cell}, V) is calculated as the sum of equilibrium potential (E_{eq}, V), membrane potential (E_m, V), and ohmic losses (E_{ohmic}, V).

$$E_{cell} = E_{eq} + E_m + E_{ohmic} \tag{15}$$

E_{eq} is the potential invested in creating the pH difference between the anode (pH_{anode}) and cathode ($pH_{cathode}$) considering each pH unit requires 59.2 mV of potential drop:

$$E_{eq} = 0.0592 \cdot (pH_{cathode} - pH_{anode}) \tag{16}$$

E_m is the potential drop over the CEM resulted from K^+ concentration gradient:

$$E_m = \frac{R \cdot T}{F} \cdot \ln \frac{c_{K^+,2}}{c_{K^+,1}} \tag{17}$$

where $c_{K^+,2}$ is the K^+ concentration in the catholyte (mol m^{-3}).

E_{ohmic} includes the potential drops in the acidifying and cathode compartments due to ionic resistance:

$$E_{ohmic} = j_c \cdot \left(\frac{d_a}{\sigma_a} + \frac{d_c}{\sigma_c} \right) \tag{18}$$

where d_a and d_c are the thicknesses of the acidifying and cathode compartments (m), respectively, and σ_a and σ_c are the conductivities of the acidifying solution and catholyte (S m^{-1}), respectively.

Finally, the energy consumption (EC) is then calculated by:

$$EC = \frac{E_{cell} \cdot j_c}{J_{CO_2}} \tag{19}$$

3. Results and discussion

3.1. Effects of decreased CO_2 desorption pressure

In the experiments with reduced CO_2 partial pressure at the gas side ($p_{CO_2,g}$) of the membrane contactor, the energy consumption of the electrochemical system decreased with decreasing p_{CO_2} (Fig. 2). We have observed this decrease in energy consumption under applied partial vacuum with different applied current densities and different load ratios of K^+ (L_{K^+}).

The decrease in energy consumption originated from two aspects: increased CO_2 production rate and decreased cell voltage. The driving force for CO_2 desorption was the difference in CO_2 partial pressure between the liquid and gas side of the membrane contactor [30], so reducing $p_{CO_2,g}$ increased the CO_2 production rate (Fig. 3a). With $p_{CO_2,g}$ decreased from 0.9 to 0.3 atm, the benefits from increasing CO_2

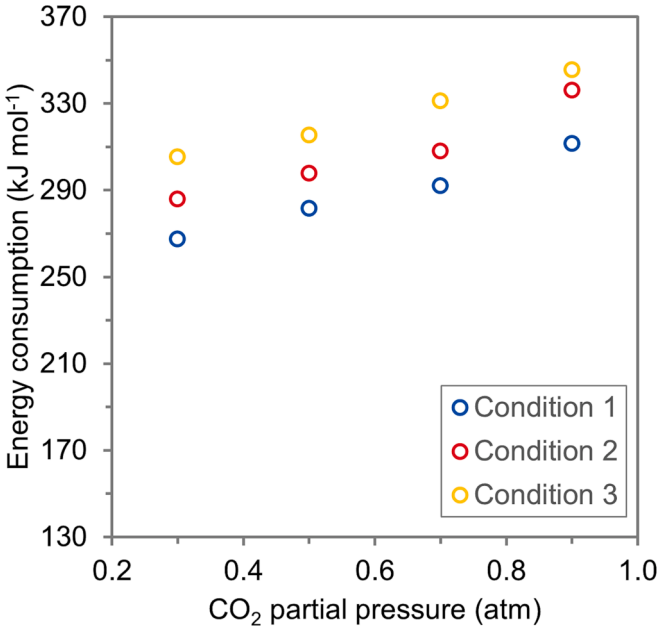

Fig. 2. Energy consumption at different CO_2 partial pressure at the gas side of the membrane contactor ($p_{CO_2,g}$). Condition 1: j_c = 150 A m^{-2}, L_{K^+} = 0.8, 0.1 M phosphate buffer; condition 2: j_c = 150 A m^{-2}, L_{K^+} = 0.9, 0.1 M phosphate buffer; condition 3: j_c = 200 A m^{-2}, L_{K^+} = 0.8, 0.1 M phosphate buffer.

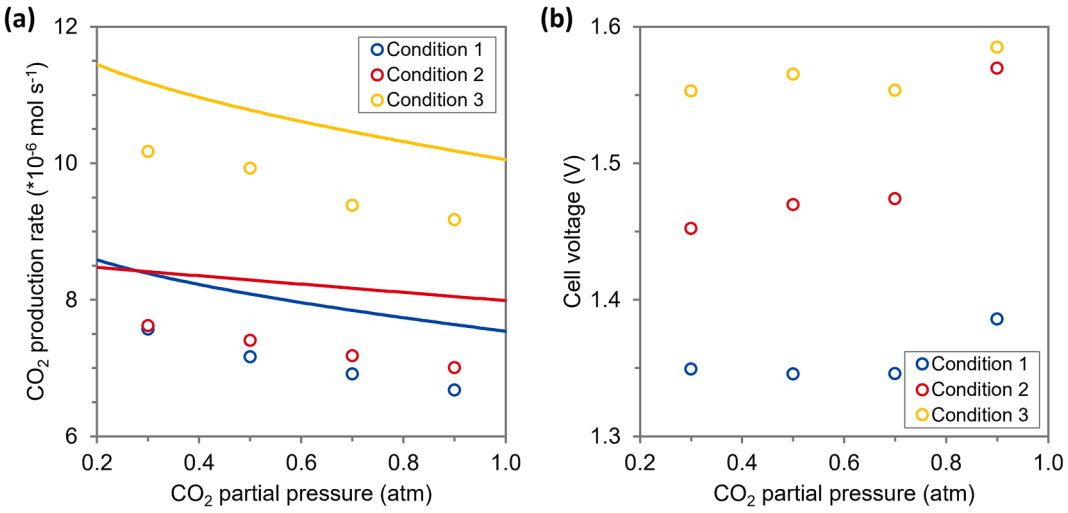

Fig. 3. Change of (a) CO_2 production rate and (b) cell voltage under different p_{CO_2} values. Condition 1: $j_c = 150$ A m^{-2}, $L_{K^+} = 0.8$, 0.1 M phosphate buffer; condition 2: $j_c = 150$ A m^{-2}, $L_{K^+} = 0.9$, 0.1 M phosphate buffer; condition 3: $j_c = 200$ A m^{-2}, $L_{K^+} = 0.8$, 0.1 M phosphate buffer. Symbols (○): experimental data; lines: model predictions.

production rate accounted for 84% of the total energy reduction at the experimental conditions with $L_{K^+} = 0.8$ (condition 1, while this benefit accounted only for 54% at condition 2 with $L_{K^+} = 0.9$. In condition 2, the pH of the acidifying solution was around 1-unit lower comparing to the acidifying solution in condition 1. The lower acidifying solution pH resulted in a higher concentration of H_2CO_3 and a higher CO_2 partial pressure in the liquid phase. Hence, the driving force for CO_2 desorption was higher under condition 2 comparing to condition 1, which led to a higher CO_2 production rate at $p_{CO_2,g} = 0.9$ atm. When $p_{CO_2,g}$ decreased to 0.3 atm, the applied partial vacuum dominated the desorption of CO_2 so that the difference in CO_2 production rate was minimized. The model results showed the same trend of CO_2 production rate change in all the conditions with different $p_{CO_2,g}$, although the overall values of the simulation were higher than the experimental results, likely due to some CO_2 leakage during experiments.

The applied partial vacuum reduced the cell voltage especially when $p_{CO_2,g}$ decreased from 0.9 to 0.7 atm (Fig. 3b). One assumption for the reduced cell voltage was that the elimination of CO_2 gas bubbles in the cell decreased the electrical resistance. Generally, the CO_2 gas formed inside the cell could be carried out instantly by the liquid flow. However, some bubbles may remain trapped in the meshed spacer, thus increasing the electrical resistance [31,32]. With a reduced pressure in the gas phase, the volumes of the gas (bubbles) formed were bigger according to ideal gas law. Therefore, the larger-volume bubbles were easier to be carried out of the cell by the liquid flow instead of being trapped in the spacer [33]. This elimination of gas bubbles occurred mainly between $p_{CO_2,g}$ of 0.9 and 0.7 atm, and further decrease of $p_{CO_2,g}$ did not have a significant impact on the cell voltage. Moreover, as the model did not include the effect of gas bubbles on cell voltage, so the results of the model simulation were not presented in the figure.

However, creating and maintaining the vacuum requires additional energy investment in operation, and low pressure of the desorbed CO_2 creates an energy penalty for the downstream processes as CO_2 needs to be pressurized for transport and storage [34,35]. The thermodynamical minimum energy required to reduce CO_2 desorption pressure from 0.9 to 0.3 atm is 2.7 kJ mol^{-1}, and the same amount of energy is required to pressurize the pure CO_2 back from 0.3 to 0.9 atm. In practice, this energy penalty is larger due to the imperfect efficiency of the vacuum pump and gas compressor, e.g., the practical energy consumption to compress CO_2 gas at lower pressure requires slightly more energy due to the larger volume of gas [36]. Nevertheless, considering an 80% efficiency of the vacuum pump and the compressor, the total energy required for the decreased CO_2 desorption pressure is about 6.8 kJ mol^{-1}, which is less than 20% of the energy saving by applying this strategy. Therefore, a decreased CO_2 desorption pressure is beneficial for reducing the overall energy consumption of the electrochemical system by increasing CO_2 production rate and decreasing cell voltage.

3.2. *Effect of phosphate buffer on cell performance*

We expected the addition of phosphate buffer to the absorbent would lower the energy consumption by reducing the ohmic resistance and the electrode overpotential. However, in this study, the energy consumption of experiments with buffer addition was not always lower than the experiments without buffer addition. Instead, adding phosphate buffer shifted the optimal L_{K^+} for the lowest energy consumption of the electrochemical cell (Fig. 4). The lowest energy consumption was achieved without adding buffer at $L_{K^+} = 1.0$, with 0.1 M buffer at $L_{K^+} = 0.8$, and with 0.2 M buffer at $L_{K^+} = 0.7$ (energy consumption of 305 kJ mol^{-1}, 267 kJ mol^{-1}, and 297 kJ mol^{-1}, respectively). This shift of optimal L_{K^+} was also observed with the model simulation where the optimal L_{K^+} value decreases with increasing buffer concentration. Overall, both experimental and model results show that the lowest energy consumption of all investigated conditions occurred with 0.1 M buffer at $L_{K^+} = 0.8$.

The energy consumption is proportional to the cell voltage and inversely proportional to the CO_2 production rate. Cell voltage increased with higher L_{K^+} owing to the lower conductivity of the acidifying solution and higher potential drop at the boundary layers of the MEA and CEM (Fig. 5a). As more K^+ ions were transported to the cathode compartment and CO_3^{2-}/HCO_3^- ions were converted to CO_2 gas, the conductivity of the acidifying solution decreased with a higher L_{K^+} (Table S2), which led to a greater ohmic loss in the cell. Moreover, this depletion of K^+ and CO_3^{2-}/HCO_3^- ions was intensified near the surface of the MEA at the acidifying compartment side, which resulted in a larger potential drop at the boundary layer of the MEA [37]. Furthermore, the K^+ concentration gradient over the CEM was larger with a higher L_{K^+} (Table S2), and this larger gradient contributed to the increase of the membrane potential of the CEM [38]. On the other hand, adding phosphate buffer provided extra conductivity in both the acidifying solution and the boundary layer of the MEA, since the anionic phosphate species remained in the acidifying solution increased the total ion concentration. Hence, we observed a lower cell voltage with more phosphate buffer added, and the difference of cell voltage was larger with a higher L_{K^+} when more K^+ and CO_3^{2-}/HCO_3^- were removed. Although Jeremiasse et al. showed a reduced concentration overpotential for

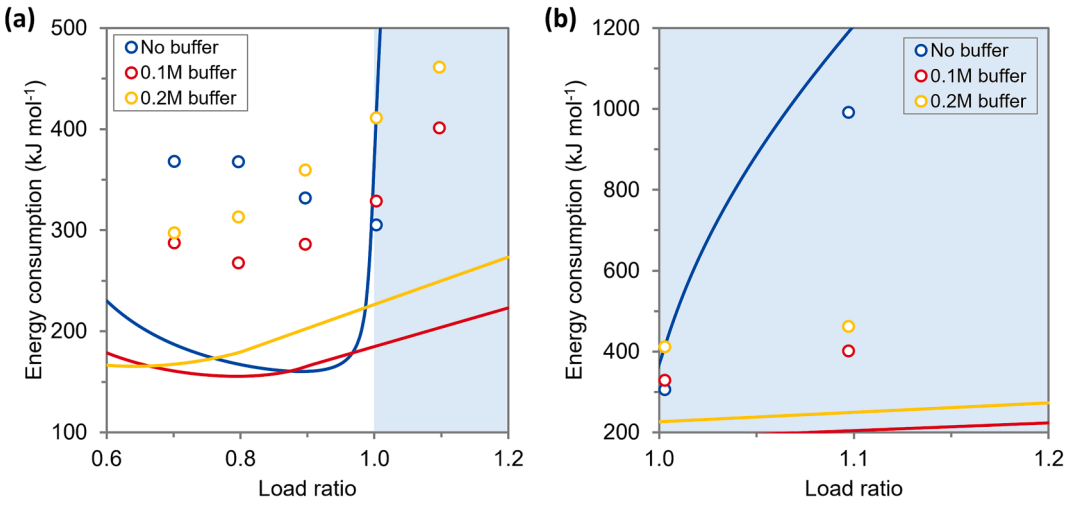

Fig. 4. Energy consumption under different load ratio and phosphate buffer concentration. (a) Load ratio range between 0.6 and 1.2, (b) a zoomed view for load ratio between 1.0 and 1.2. Symbols (○): experimental data; lines: model predictions.

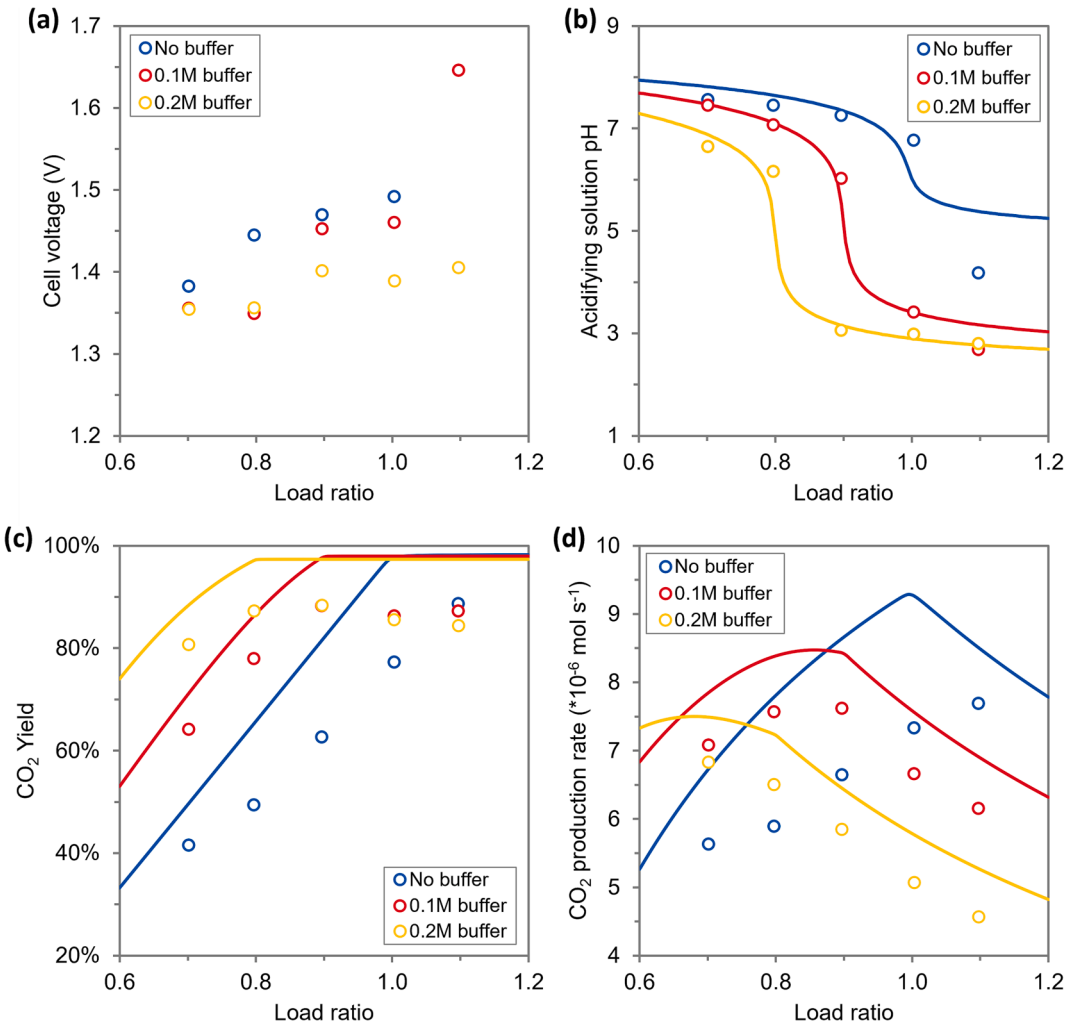

Fig. 5. Experimental and model simulated results of (a) cell voltage, (b) acidifying solution pH, (c) CO_2 yield, and (d) CO_2 production rate under different load ratio and phosphate buffer concentration. Symbols (○): experimental data; lines: model predictions.

hydrogen evolution with phosphate buffer addition [29], this reduction was not evident in our experiments due to the extreme catholyte pH (>13). The small fluctuation of the cathode overpotential (Table S3) could be explained by the influence of hydrogen gas bubbles on the cathode potential measurement [33].

The protons produced at the anode were transported to the acidi-

fying compartment under the applied constant current, which led to the decrease of the acidifying solution pH. The steady-state pH of the acidifying solution decreased at a higher L_{K^+} (Fig. 5b), which was attributed to more protons received by each unit volume of acidifying solution. This decrease in pH was not linear to the increase in L_{K^+} due to the buffering effect of CO_3^{2-}/HCO_3^- ions and/or the added phosphate buffer. In the experiments without buffer, the acidifying solution needed to overcome two buffering zones of CO_3^{2-}/HCO_3^- ($pK_a = 10.33$ and 6.35). The concentration of CO_3^{2-}/HCO_3^- ions was reduced in the experiments with phosphate buffer since the total K^+ concentration in the influent was remained constant in all the experiments. Moreover, phosphate buffer only has one buffering zone ($pK_a = 7.20$) in the pH range of the desired pH swing in the acidifying solution. As a result, the addition of phosphate buffer solution decreased the steady-state pH of the acidifying solution. This conclusion also explains the discrepancy between the experimental and simulated acidifying solution pH at $L_{K^+} = 1.1$ with no buffer addition, as any background anions "contamination" in the experiments would decrease the acidifying solution pH.

Due to the displacement of CO_2 equilibria, more CO_2 could be evolved with a lower pH of the acidifying solution. Thus, the CO_2 yield, which is defined as the ratio of CO_2 gas production rate to the total carbon feeding rate into the cell, followed a reverse trend to the pH of the acidifying solution (Fig. 5c). The yield reached its maximum when all the dissolved carbon species had been converted to H_2CO_3 at around pH = 4. At $p_{CO_2,g} = 0.3$ atm, the concentration of H_2CO_3 in the acidifying solution was 10.2 mM based on Henry's law. This 10.2 mM of H_2CO_3 could not be desorbed into the gas phase even with further decrease of the acidifying solution pH at higher L_{K^+}, so the yield kept constant at the maximum. Due to less total carbon in the influent of experiments with phosphate buffer, the remained H_2CO_3 accounted for a larger portion in these experiments. Hence, the maximum CO_2 yield decreased with increasing concentration of phosphate buffer.

Although the CO_2 yield was proportional to the CO_2 production rate, the change of the CO_2 production rate did not follow the same trend as the CO_2 yield, due to the variation of the total carbon feeding rate (Fig. 5d). In experiments with the same buffer concentration, the total carbon feeding rate decreased with higher L_{K^+} attributed to the lower flow rate of the influent (1.33 mL min^{-1} at $L_{K^+} = 0.7$ while 0.85 mL min^{-1} at $L_{K^+} = 1.1$). Consequently, the CO_2 production rate decreased sharply after the CO_2 yield reached the maximum. Moreover, the total carbon feeding rate decreased by 19% and 38% with 0.1 M and 0.2 M phosphate buffer added, respectively. Therefore, the CO_2 production rate of the experiments without buffer addition exceeded those of the experiments with buffer added at higher L_{K^+}.

As shown in Fig. 4, the experiments with no buffer addition had the lowest energy consumption at $L_{K^+} = 1.0$, which was lower than in the experiments with buffer addition at the same L_{K^+}. However, the buffer addition limited the total carbon feeding rate. Thus, we have also performed experiments with fixed total carbon feeding rate (Table 2). The lowest energy consumption was achieved with 0.1 M phosphate buffer added, which was confirmed by the model simulation (617 kJ mol^{-1} without buffer, 156 kJ mol^{-1} with 0.1 M buffer, 160 kJ mol^{-1} with 0.2 M buffer). Adding phosphate provided extra conductivity in the acidifying compartment and lowered the L_{K^+} due to the increasing influent K^+ concentration, so the cell voltage was lower with more buffer added.

Table 2
Experimental conditions and results of the experiments with fixed total carbon feeding rate.

	No buffer	0.1 M buffer	0.2 M buffer
Total carbon feeding rate (mol s^{-1})	9.5×10^{-6}	9.5×10^{-6}	9.5×10^{-6}
L_{K^+}	1.00	0.84	0.72
Energy consumption (kJ mol^{-1})	305	273	286
Cell voltage (V)	1.49	1.38	1.35
Acidifying solution pH	6.8	6.8	7.3
CO_2 production rate (mol s^{-1})	7.3×10^{-6}	7.6×10^{-6}	7.1×10^{-6}

Moreover, the acidifying solution pH was comparable between the experiment without buffer and with 0.1 M buffer, but the CO_2 production rate with 0.1 M buffer was 4% higher, which indicated that adding phosphate buffer facilitated the desorption of CO_2 gas. However, in the experiment with 0.2 M buffer, the CO_2 production rate was the lowest due to the higher acidifying solution pH at a relatively low L_{K^+}.

3.3. Effects of adding sulphate solution

As the previous section concludes, adding 0.1 M phosphate buffer reduced the energy consumption of the electrochemical system, where phosphate essentially acts as a supporting electrolyte in the system. In fact, adding sulphate to the absorbent reduced the energy consumption even further, while the energy consumption trend with different L_{K^+} is the same with both phosphate and sulphate (Fig. 6). Thus, among all the investigated experimental conditions, the lowest energy consumption was 247 kJ mol^{-1} achieved at $p_{CO_2,g} = 0.3$ atm, $L_{K^+} = 0.8$, $j_c = 150$ A m^{-2}, and with 0.1 M of sulphate addition. The model predicted the lowest energy consumption of 138 kJ mol^{-1} under the same condition, while the difference between the experiment and the simulation could be attributed to electrode overpotentials and CO_2 leakage (which were not covered by the model).

Firstly, while phosphate buffer has one buffering zone in the pH range of the acidifying solution, sulphate does not have any buffer capacity. As a result, the pH of acidifying solution under the same L_{K^+} was lower with sulphate addition than with phosphate addition (Fig. 7a). At $L_{K^+} < 0.9$, the lower pH favored the desorption of CO_2 so that the CO_2 production rate was higher with sulphate addition (Fig. 7b). However, when the pH of acidifying solution was lower than 4, the CO_2 yield reached its maximum, and the CO_2 production rate was limited by the total carbon feeding rate. Therefore, the CO_2 production rate was equivalent with different electrolytes addition at $L_{K^+} \geq 0.9$. Secondly, the cell voltage only showed differences at $L_{K^+} > 0.8$ between sulphate addition and phosphate addition (Fig. 7c). As discussed before, the benefit of adding phosphate buffer was primarily to increase the conductivity in the acidifying compartment provided by phosphate. Moreover, sulphate ions have higher molar conductivity comparing to HPO_4^{2-} and $H_2PO_4^-$ (i.e., the main phosphate species in the pH range of the

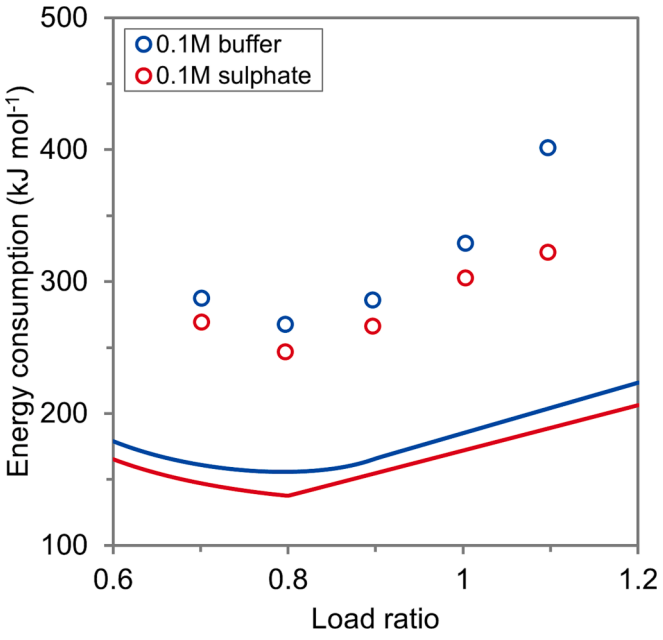

Fig. 6. Energy consumption under different load ratio with 0.1 M of phosphate buffer or 0.1 M of sulphate added. Symbols (○): experimental data; lines: model simulation results.

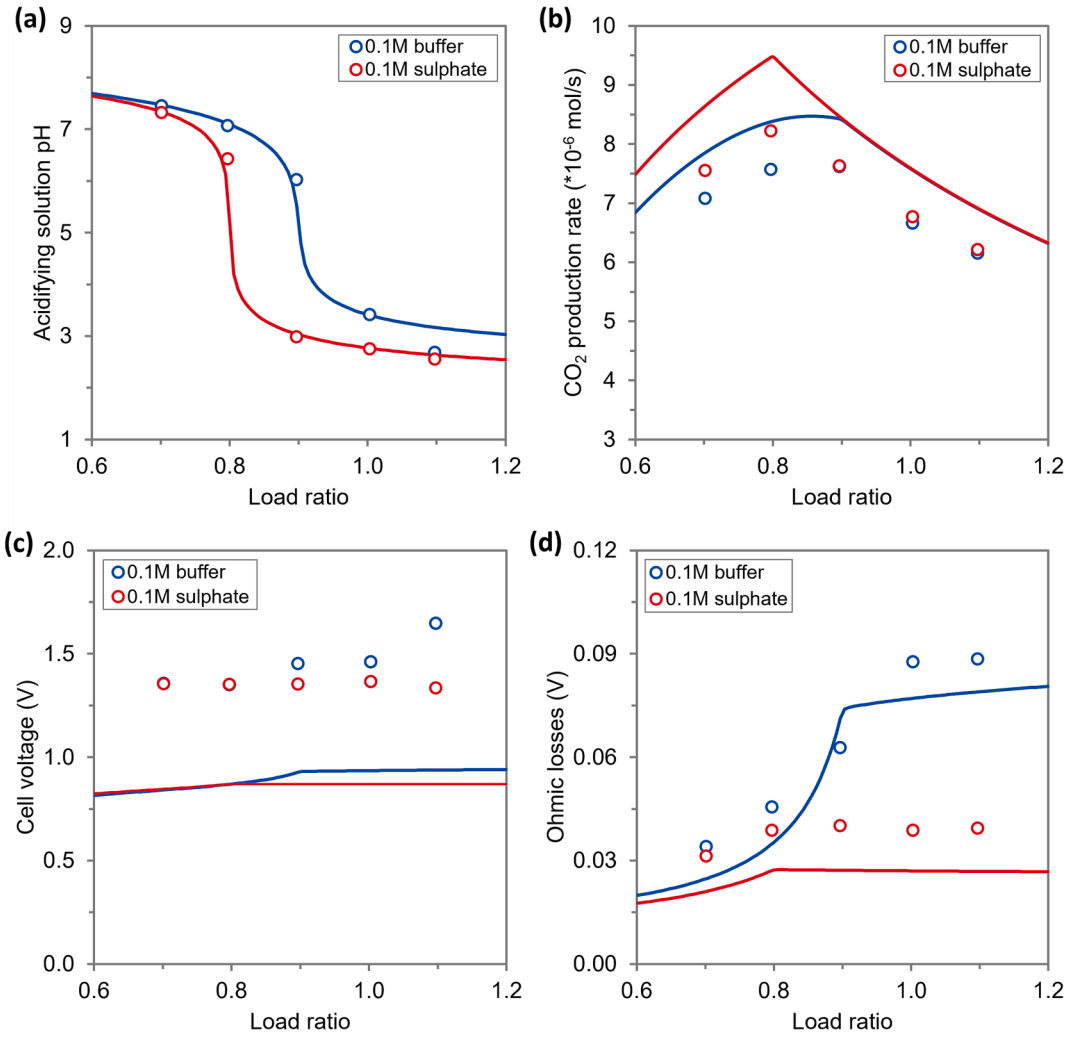

Fig. 7. Experimental and model simulated results of (a) acidifying solution pH, (b) CO_2 production rate, (c) cell voltage, and (d) ohmic losses under different load ratio with 0.1 M phosphate buffer or 0.1 M sulphate addition. Symbols (○): experimental data; lines: model simulation results.

acidifying solution). Furthermore, the impact of the ionic conductivity was higher at high L_{K^+} when the acidifying solution was more depleted. Hence, the ohmic losses originated from the ionic resistance was lower when adding sulphate than with phosphate at $L_{K^+} > 0.8$ (Fig. 7d). The difference in ohmic losses accounted for 23%, 51%, and 16% of the cell voltage difference at $L_{K^+} = 0.9$, 1.0, and 1.1, respectively. The rest of the cell voltage difference between different electrolytes addition could be explained by the boundary effects on the surface of the MEA. On the surface of the acidifying compartment side of the MEA, the K^+ concentration decreased and H^+ concentration increased with higher L_{K^+}, which induced a lower local pH. Driven by the current applied, the anionic species moved towards the surface of the MEA. As discussed before, without the addition of buffer or sulphate, due to the formation of non-conductive H_2CO_3, the boundary layer of the MEA provided a high potential drop. While H_3PO_4 has a lower pK_a than H_2CO_3 (2.10 vs 6.35), more charged phosphate species ($H_2PO_4^-$/HPO_4^{2-}) could be present at the boundary layer and provide conductivity. Moreover, H_2SO_4, as a strong acid, has a pKa of −2.80, so all the sulphate species at the boundary layer were in charged dissociated form. Therefore, adsorbent with sulphate addition reduced the potential drop at the boundary layer of the MEA, which led to the lower cell voltage.

Overall, we have achieved a reduction of approximately 30% in energy consumption by adding 0.1 M sulphate comparing to no background electrolyte addition at $L_{K^+} = 0.8$. Sabatino et al. have performed a techno-economic analysis of bipolar membrane electrodialysis for direct air capture processes [28]. They reviewed several solutions for reducing the energy consumption of the electrochemical process, and one of the solutions was addition of an inert salt to the solvent. This solution was simulated by a mathematical model and resulted in a maximum energy reduction of ~ 29%. Therefore, our experimental results showed comparable reduction in the energy consumption by adding background electrolytes.

4. Conclusions

In this work, we have shown different strategies to reduce the energy consumption for the electrochemical DAC process by decreasing the CO_2 desorption pressure and adding background electrolyte. When the CO_2 partial pressure at the gas phase of the membrane contactor was reduced from 0.9 to 0.3 atm, the energy consumption of the process decreased 12 to 15% among the three tested conditions. The applied partial vacuum increased the CO_2 production rate by increasing the driving force for CO_2 desorption from liquid to gas and decreased the cell voltage by diminishing gas bubbles in the electrochemical cell. Moreover, the addition of 0.1 and 0.2 M of phosphate changed the optimum L_{K^+}, where we observed the lowest energy consumption at $L_{K^+} = 0.8$ with 0.1 M buffer. The addition of the phosphate buffer increased the conductivity of both the acidifying solution and the boundary layer of the MEA, so the cell voltage decreased with more buffer added. However, the CO_2 production rate was limited by either the total carbon feeding rate with

higher buffer concentration at fixed influent K^+ concentration or a higher acidifying solution pH with higher buffer concentration at fixed total carbon feeding rate. Finally, because of the low pKa and high molar conductivity of sulphate comparing to phosphate, 0.1 M sulphate addition showed lower energy consumption than 0.1 M phosphate addition at the same L_{K^+}. Among all the investigated conditions, the lowest energy consumption was 247 kJ mol^{-1} achieved at $p_{CO_2,g} = 0.3$ atm, $L_{K^+} = 0.8$, $j_c = 150$ A m^{-2} with 0.1 M of sulphate addition, while the model predicted the minimum of 138 kJ mol^{-1} under the same condition. The experimental lowest energy consumption of this work is 34% lower comparing to our previous work, which makes this electrochemical process more competitive among all the DAC technologies.

Declaration of Competing Interest

The authors declare that they have no known competing financial interests or personal relationships that could have appeared to influence the work reported in this paper.

Data availability

The research data underlying this work can be found online at https://doi.org/10.4121/22140593.

Acknowledgements

This work was performed in the cooperation framework of Wetsus, European Centre of Excellence for Sustainable Water Technology (www.wetsus.eu). Wetsus is co-funded by the Dutch Ministry of Economic Affairs and Ministry of Infrastructure and Environment, the European Union Regional Development Fund, the Province of Fryslân, and the Northern Netherlands Provinces. The authors would like to thank the participants of the research theme "Sustainable Carbon Cycle" for fruitful discussions and financial support and Mr. John Ferwerda for the technical support.

Appendix A. Supplementary data

Supplementary data to this article can be found online at https://doi.org/10.1016/j.cej.2023.144251.

References

[1] IPCC, Climate Change 2022: Mitigation of Climate Change. Contribution of Working Group III to the Sixth Assessment Report of the Intergovernmental Panel on Climate Change, 2022. https://doi.org/10.1017/9781009157926.
[2] Carbon Dioxide | Vital Signs – Climate Change: Vital Signs of the Planet, (n.d.). https://climate.nasa.gov/vital-signs/carbon-dioxide/ (accessed October 4, 2022).
[3] J.H. Mercer, West Antarctic ice sheet and CO2 greenhouse effect: a threat of disaster, Nature 271 (1978) 321–325, https://doi.org/10.1038/271321a0.
[4] G.L. Foster, E.J. Rohling, Relationship between sea level and climate forcing by CO 2 on geological timescales, Proc. Natl. Acad. Sci. U.S.A. 110 (4) (2013) 1209–1214.
[5] M.C. Urban, Accelerating extinction risk from climate change, Science 348 (2015) (1979) 571–573, https://doi.org/10.1126/science.aaa4984.
[6] Á. Galán-Martín, D. Vázquez, S. Cobo, N. Mac Dowell, J.A. Caballero, G. Guillén-Gosálbez, Delaying carbon dioxide removal in the European Union puts climate targets at risk, Nat Commun. 12 (2021) 6490, https://doi.org/10.1038/s41467-021-26680-3.
[7] T. Gasser, C. Guivarch, K. Tachiiri, C.D. Jones, P. Ciais, Negative emissions physically needed to keep global warming below 2 °C, Nat Commun. 6 (2015) 7958, https://doi.org/10.1038/ncomms8958.
[8] D.P. van Vuuren, S. Deetman, J. van Vliet, M. van den Berg, B.J. van Ruijven, B. Koelbl, The role of negative CO2 emissions for reaching 2 °C—insights from integrated assessment modelling, Clim Change. 118 (2013) 15–27, https://doi.org/10.1007/s10584-012-0680-5.
[9] E.S. Sanz-Pérez, C.R. Murdock, S.A. Didas, C.W. Jones, Direct Capture of CO2 from Ambient Air, Chem Rev. 116 (2016) 11840–11876, https://doi.org/10.1021/acs.chemrev.6b00173.
[10] M. Erans, E.S. Sanz-Pérez, D.P. Hanak, Z. Clulow, D.M. Reiner, G.A. Mutch, Direct air capture: process technology, techno-economic and socio-political challenges, Energy, Environ Sci. 15 (2022) 1360–1405, https://doi.org/10.1039/D1EE03523A.
[11] J. Elfving, J. Kauppinen, M. Jegoroff, V. Ruuskanen, L. Järvinen, T. Sainio, Experimental comparison of regeneration methods for CO2 concentration from air using amine-based adsorbent, Chem. Eng. J. 404 (2021), 126337, https://doi.org/10.1016/J.CEJ.2020.126337.
[12] R. Hanna, A. Abdulla, Y. Xu, D.G. Victor, Emergency deployment of direct air capture as a response to the climate crisis, Nat Commun. 12 (2021) 368, https://doi.org/10.1038/s41467-020-20437-0.
[13] C. Breyer, M. Fasihi, C. Bajamundi, F. Creutzig, Direct Air Capture of CO2: A Key Technology for Ambitious Climate Change Mitigation, Joule. 3 (2019) 2053–2057, https://doi.org/10.1016/J.JOULE.2019.08.010.
[14] D.W. Keith, G. Holmes, D. St. Angelo, K. Heidel, A Process for Capturing CO2 from the Atmosphere, A Process for Capturing CO2 from the Atmosphere, Joule. 2 (8) (2018) 1573–1594.
[15] R. Sharifian, R.M. Wagterveld, I.A. Digdaya, C. Xiang, D.A. Vermaas, Electrochemical carbon dioxide capture to close the carbon cycle, Energy, Environ Sci. 14 (2021) 781–814, https://doi.org/10.1039/D0EE03382K.
[16] R.J. Gilliam, B.K. Boggs, V. Decker, M.A. Kostowskyj, S. Gorer, T.A. Albrecht, J. D. Way, D.W. Kirk, A.J. Bard, Low Voltage Electrochemical Process for Direct Carbon Dioxide Sequestration, J Electrochem Soc. 159 (2012) B627–B628, https://doi.org/10.1149/2.033206jes.
[17] C. Jiang, S. Li, D. Zhang, Z. Yang, D. Yu, X. Chen, Y. Wang, T. Xu, Mathematical modelling and experimental investigation of CO2 absorber recovery using an electro-acidification method, Chem. Eng. J. 360 (2019) 654–664, https://doi.org/10.1016/J.CEJ.2018.12.006.
[18] S. Jin, M. Wu, Y. Jing, R.G. Gordon, M.J. Aziz, Low energy carbon capture via electrochemically induced pH swing with electrochemical rebalancing, Nat Commun 13 (1) (2022) 1–11, https://doi.org/10.1038/s41467-022-29791-7.
[19] M.D. Eisaman, L. Alvarado, D. Larner, P. Wang, B. Garg, K.A. Littau, CO2 separation using bipolar membrane electrodialysis, Energy, Environ Sci. 4 (2011) 1319–1328, https://doi.org/10.1039/C0EE00303D.
[20] A. Iizuka, K. Hashimoto, H. Nagasawa, K. Kumagai, Y. Yanagisawa, A. Yamasaki, Carbon dioxide recovery from carbonate solutions using bipolar membrane electrodialysis, Sep Purif Technol. 101 (2012) 49–59, https://doi.org/10.1016/J.SEPPUR.2012.09.016.
[21] W. Ye, J. Huang, J. Lin, X. Zhang, J. Shen, P. Luis, B. Van Der Bruggen, Environmental evaluation of bipolar membrane electrodialysis for NaOH production from wastewater: Conditioning NaOH as a CO2 absorbent, Sep Purif Technol. 144 (2015) 206–214, https://doi.org/10.1016/J.SEPPUR.2015.02.031.
[22] S. Valluri, S.K. Kawatra, Reduced reagent regeneration energy for CO2 capture with bipolar membrane electrodialysis, Fuel Process. Technol. 213 (2021), 106691, https://doi.org/10.1016/J.FUPROC.2020.106691.
[23] Q. Shu, L. Legrand, P. Kuntke, M. Tedesco, H.V.M. Hamelers, Electrochemical Regeneration of Spent Alkaline Absorbent from Direct Air Capture, Environ Sci Technol. 54 (2020) 8990–8998, https://doi.org/10.1021/acs.est.0c01977.
[24] Q. Shu, M. Haug, M. Tedesco, P. Kuntke, H.V.M. Hamelers, Direct Air Capture Using Electrochemically Regenerated Anion Exchange Resins, Environ Sci Technol. 56 (2022) 11559–11566, https://doi.org/10.1021/acs.est.2c01944.
[25] F. Sabatino, M. Mehta, A. Grimm, M. Gazzani, F. Gallucci, G. Jan Kramer, M. van Sint Annaland, Evaluation of a Direct Air Capture Process Combining Wet Scrubbing and Bipolar Membrane Electrodialysis, Ind Eng Chem Res. 59 (2020) 7007–7020, https://doi.org/10.1021/acs.iecr.9b05641.
[26] M. Fang, Z. Wang, S. Yan, Q. Cen, Z. Luo, CO2 desorption from rich alkanolamine solution by using membrane vacuum regeneration technology, Int. J. Greenhouse Gas Control 9 (2012) 507–521, https://doi.org/10.1016/J.IJGGC.2012.05.013.
[27] Z. Wang, M. Fang, Q. Ma, Z. Zhao, T. Wang, Z. Luo, Membrane Stripping Technology for CO2 Desorption from CO2-rich Absorbents with Low Energy Consumption, Energy Procedia 63 (2014) 765–772, https://doi.org/10.1016/J.EGYPRO.2014.11.085.
[28] F. Sabatino, M. Gazzani, F. Gallucci, M. van Sint Annaland, Modeling, Optimization, and Techno-Economic Analysis of Bipolar Membrane Electrodialysis for Direct Air Capture Processes, Ind Eng Chem Res. 61 (34) (2022) 12668–12679.
[29] A.W. Jeremiasse, H.V.M. Hamelers, J. Mieke Kleijn, C.J.N. Buisman, Use of Biocompatible Buffers to Reduce the Concentration Overpotential for Hydrogen Evolution, Environ Sci Technol. 43 (2009) 6882–6887, https://doi.org/10.1021/es9008823.
[30] Z.G. Peng, S.H. Lee, T. Zhou, J.J. Shieh, T.S. Chung, A study on pilot-scale degassing by polypropylene (PP) hollow fiber membrane contactors, Desalination 234 (2008) 316–322, https://doi.org/10.1016/J.DESAL.2007.09.100.
[31] A. Angulo, P. van der Linde, H. Gardeniers, M. Modestino, D. Fernández Rivas, Influence of Bubbles on the Energy Conversion Efficiency of Electrochemical Reactors, Joule. 4 (2020) 555–579, https://doi.org/10.1016/J.JOULE.2020.01.005.
[32] X. Zhao, H. Ren, L. Luo, Gas Bubbles in Electrochemical Gas Evolution Reactions, Langmuir 35 (2019) 5392–5408, https://doi.org/10.1021/acs.langmuir.9b00119.
[33] A. Taqieddin, R. Nazari, L. Rajic, A. Alshawabkeh, Review—Physicochemical Hydrodynamics of Gas Bubbles in Two Phase Electrochemical Systems, J Electrochem Soc. 164 (2017) E448–E459, https://doi.org/10.1149/2.1161713jes.
[34] V.E. Onyebuchi, A. Kolios, D.P. Hanak, C. Biliyok, V. Manovic, A systematic review of key challenges of CO2 transport via pipelines, Renew. Sustain. Energy Rev. 81 (2018) 2563–2583, https://doi.org/10.1016/J.RSER.2017.06.064.
[35] M.D. Aminu, S.A. Nabavi, C.A. Rochelle, V. Manovic, A review of developments in carbon dioxide storage, Appl Energy. 208 (2017) 1389–1419, https://doi.org/10.1016/J.APENERGY.2017.09.015.

[36] J.D. Van de Ven, P.Y. Li, Liquid piston gas compression, Appl Energy. 86 (2009) 2183–2191, https://doi.org/10.1016/J.APENERGY.2008.12.001.
[37] J.J. Krol, M. Wessling, H. Strathmann, Concentration polarization with monopolar ion exchange membranes: current–voltage curves and water dissociation, J Memb Sci. 162 (1999) 145–154, https://doi.org/10.1016/S0376-7388(99)00133-7.
[38] T. Luo, S. Abdu, M. Wessling, Selectivity of ion exchange membranes: A review, J Memb Sci. 555 (2018) 429–454, https://doi.org/10.1016/J.MEMSCI.2018.03.051.